Dynamics and rheological properties of suspensions of paramagnetic spherical particles under constant magnetic fields

Mingyang Tan ⬤

Polymer Program, Institute of Materials Science, University of Connecticut, Storrs, Connecticut 06084, USA

Joshua A. Adeniran ⬤ and Travis W. Walker ⬤*

Karen M. Swindler Department of Chemical and Biological Engineering, South Dakota School of Mines & Technology, Rapid City, South Dakota 57701, USA

Magnetorheological fluids span an astounding range of applications. Investigating such systems provides insight into the relationships between the rheological properties and the imposed flow and magnetic conditions, thus aiding in the processing of the magnetorheological fluids. In this study, we apply an in-house Stokesian dynamics code to investigate the dynamics, microstructures, and rheological properties of magnetorheological fluids under constant magnetic fields with different directions and magnitudes. A spectral Ewald method is applied to improve the computational capability. Constrained two-dimensional and fully three-dimensional simulations are conducted, and the results are compared. A magnetic-thickening phenomenon is observed in both the constrained two-dimensional and fully three-dimensional simulations, when the magnetic field is in the shear-flow-gradient direction. However, a magnetic-thickening phenomenon is observed in the constrained two-dimensional simulation while a magnetic-thinning phenomenon is observed in the fully three-dimensional simulation when the field is in the shear-flow direction.

I. INTRODUCTION

Magnetorheological (MR) fluids and electrorheological (ER) fluids are composed of paramagnetic or dielectric particles and a solvent. They have drawn extensive interest since the first introduction by Rabinow [1] (MR fluid) and Winslow [2] (ER fluid). Upon an application of an external field, the interactions between the induced dipoles of the particles cause clusterings of particles. Formations of structures that are subject to external fields result in changes of apparent viscosity over several orders of magnitude, and these changes are often rapid and reversible. This intriguing property causes MR and ER fluids to be great candidates for applications that require controllable mechanical strength, such as shock absorbers and dampers. External magnetic or electric fields can also control the crystal structures as well as the resulting transport and optical properties, which makes such suspensions appealing for fabrications of composites by self-assemblies of particles. Examples include one-dimensional assembly into microwires [3,4], two-dimensional assembly into hexagonal sheets [5–7] and asters [8], and three-dimensional assembly into superlattices [9]. The active response of a particle to an external field also makes particle assembly appealing for artificial microswimmers [10–12].

Properties of suspensions of paramagnetic particles at equilibrium, such as particle distribution, permeability or conductivity, and optical responses, depend on the balance among external forces,

---

*travis.walker@sdsmt.edu

043701-1

interparticle forces, and Brownian effects. Thus, a theoretical and numerical prediction of the equilibrium properties depends largely on the description of the magnetic interactions between particles. An exact calculation of the magnetic forces of particles requires a solution to the Laplace equation of potential with appropriate boundary conditions [13]. The field is formulated by taking the gradient of the potential and is utilized to construct the Maxwell stress tensor. The magnetic force is then calculated as an integration of the Maxwell stress tensor over the surface of the particle. This method includes both many-body interactions and multipoles, but it bears the cumbersomeness that is not suitable for simulations of a large number of particles. In fact, analytic expressions only exist for a small number of particles with highly symmetric configurations [14,15]. As an alternative, only dipolar interactions are considered in most theoretical and numerical studies. Among those studies, the *fixed-dipole* model is the most widely used one because of its simplicity [16–25]. In the fixed-dipole model, the particles are considered to only be induced by an external field; thus, the dipoles are treated as constants, independent of the configurations of particles. The fixed-dipole model neglects many-body interactions, and it is only accurate at large particle separations or low volume fraction of particle suspensions.

A more accurate model, the *mutual-dipole* model [26], assumes that a particle is not only induced by an external field but also by its neighboring particles. A disturbance to the magnetic field is generated by a distribution of dipoles, and each dipole is affected by the magnetic field. The dipole and magnetic field are therefore obtained simultaneously by solving a linear system that involves matrix inversion. The high computational cost of the mutual-dipole model prohibits its extensive use, but algorithms can be modified to improve the computational efficiency, and a modified algorithm will be discussed later in this work.

The mutual-dipole model has shown better accuracy than the fixed-dipole model at closer particle-particle separations [15], and the predictions of phase behavior of crystal structures of particles at equilibrium have shown very different results when comparing these two models. The phase behavior that is modeled by the fixed-dipole model is predicted to be identical for particles with different susceptibilities [27,28]. But, the mutual-dipole model predicts different phase behavior for particles with different susceptibilities [29].

Beside the models that are introduced above, Keaveny and Maxey [15] introduced a finite-dipole model by replacing the point dipole with a Gaussian kernel, Klingenberg *et al.* [30] combined the fixed-dipole model with an *ad hoc* pairwise additive magnetic force as a correction for closely separated particles, and Bonnecaze and Brady [31,32] constructed a capacitance tensor that includes both a far-field part that accounts for many-body interactions and a near-field part that accounts for higher multipoles. The algorithm by Bonnecaze and Brady [31,32] is similar to the hydrodynamic model of *Stokesian dynamics* [33–36], which will be discussed in detail later.

Nonequilibrium properties, such as dynamical and rheological properties, depend not only on the interactions that are caused by external forces, interparticle forces, and Brownian effects but also on hydrodynamic interactions. An accurate description of the hydrodynamic interactions becomes crucial in predicting the dynamical and rheological properties of suspensions of magnetic particles. Among many numerical techniques, such as the lattice Boltzmann method (LBM) [37], the boundary element method (BEM) [38], the direct numerical simulations (DNS) [39], and so on, Stokesian dynamics [35] has been successfully implemented in many numerical studies of rheological properties of colloidal suspensions on account of its accuracy and efficiency. Stokesian dynamics is a molecular-dynamics-like method that does not require resolving discretization of a fluid domain or the boundaries of the particles. In Stokesian dynamics, many-body interactions are calculated by constructing a far-field mobility tensor, while two-body interactions that account for near-field couplings are added in a pair-wise manner [33]. Although Stokesian dynamics bears the complexity of manipulations of large dense matrices, this complexity can be alleviated by using iterative schemes, such as the Krylov subspace method [40], that are combined with particle-mesh techniques in later works by Brady and his coworkers [41–43].

Either computational studies of MR fluids utilize simplified electromagnetic and/or hydrodynamic models [16–22] that cannot capture the nonequilibrium structures accurately, or they utilize

accurate models that are limited to small-scale simulations [32,44]. In this work, we use the mutual-dipole model [15,29] and the Stokesian dynamics [35,41] method to simulate the dynamics of magnetic suspensions that neglect Brownian motions and to calculate the rheological properties of such suspensions. The *spectral-Ewald* (SE) method is utilized in calculating both magnetic interactions and far-field hydrodynamic interactions in this work. The spectral Ewald method has been successfully implemented in hydrodynamics [43,45], and unlike other particle-mesh techniques such as particle mesh Ewald (PME) [46], particle-particle-particle-mesh (P^3M) [47], and smooth particle mesh Ewald (SPME) [48], SE is spectrally accurate, and it can separate the error of truncation of the wave-space sum from the error of meshing. The remainder of this paper is organized as follows. Section II introduces the mutual-dipole model and the spectral-Ewald method that solves the magnetic interactions, Sec. III introduces the Stokesian dynamics and the dynamical system of this study, Sec. IV presents the results of a numerical simulation, and Sec. V summarizes this work and outlines future directions.

II. MUTUAL-DIPOLE MODEL AND SPECTRAL EWALD

A disturbance to the magnetic field B' that is caused by a distribution of N point dipoles can be expressed as

$$B'(x) = \frac{\mu_0}{4\pi} \sum_{i=1}^{N} G(x - x_i) \cdot m_i, \tag{1}$$

where μ_0 is the free-space permeability, x is the position in space, x_i is the position of the point dipole m_i, and $G(x - x_i)$ is the propagator of the dipole when the solution to the Maxwell equations is written as a multipole expansion [49] such that

$$G(x - x_i) = \nabla\nabla \frac{1}{|x - x_i|} = \frac{3(x - x_i)(x - x_i)}{|x - x_i|^5} - \frac{I}{|x - x_i|^3}, \tag{2}$$

where I is the identity matrix.

The dipole of a particle is induced by both the external magnetic field B^∞ and the disturbance magnetic field B' such that

$$m_i = 4\pi a^3 \frac{\chi}{\mu_0} \left(B^\infty + \frac{\mu_0}{4\pi} \sum_{j=1}^{N}{}' G(x_i - x_j) \cdot m_j \right), \tag{3}$$

where a is radius of the particle, χ is the effective susceptibility, and the prime sign beside the summation means that $j = i$ is excluded from the summation. The effective susceptibility is given by

$$\chi = \frac{\mu/\mu_0 - 1}{\mu/\mu_0 + 2}, \tag{4}$$

where μ is the permeability of the particle. To obtain the dipole of a particle requires that Eq. (1) and Eq. (3) are to be solved simultaneously. After combining Eq. (1) and Eq. (3) and rearranging (putting B^∞ to one side of the equation), the relation between m_i and B^∞ becomes

$$\mathcal{B}^\infty = \Phi^\infty \cdot m, \tag{5}$$

where $\mathcal{B} = [(B^\infty)^T, (B^\infty)^T, \ldots]^T$, $m = [m_1^T, \ldots, m_N^T]^T$, and Φ^∞ is the potential tensor such that

$$\Phi^\infty = \begin{cases} \frac{\mu_0}{4\pi a^3 \chi} I & i = j \\ -\frac{\mu_0}{4\pi} G(x_i - x_j) & i \neq j \end{cases}. \tag{6}$$

The infinity sign on Φ^∞ means that the particles are treated as point particles, and only the far-field interactions are considered here. The potential tensor is to be inverted every time step in a dynamic

simulation, and it is the source of the complexity $[O(N^3)]$ of the mutual-dipole model. The inversion of the potential tensor is equivalent to an infinite summation of the reflections for the disturbance field between particles, so the mutual-dipole model accounts for many-body interactions. The same statement is justified in Stokesian dynamics [33]. Iterative schemes such as the Krylov subspace method (e.g., conjugate gradient, GMRES, etc.) can be utilized to replace the direct inversion, and the computational complexity is reduced to $O(N^2)$, which is still superlinear. The remainder of this section discusses the technique that is implemented to further reduce the computational complexity.

When calculating the macroscopic properties of a suspension, virtual boundaries may introduce the problem of interfacial effects. To overcome these effects, periodic boundary conditions are often implemented so that the space is occupied by infinite self-replications of an orthorhombic lattice. Thus, a particle inside the lattice does not only interact with other particles in the same lattice, but it also interacts with particles, including the particle itself, in image lattices. In a periodic domain, the magnetic field [Eq. (5)] can be rewritten as

$$\boldsymbol{B}^\infty = \frac{\mu_0}{4\pi a^3 \chi}\boldsymbol{m}_i - \frac{\mu_0}{4\pi}\sum_{\boldsymbol{p}}\sum_{j=1}^{N}{}^{'}\boldsymbol{G}(\boldsymbol{x}_i - \boldsymbol{x}_j + \boldsymbol{p})\cdot\boldsymbol{m}_j, \tag{7}$$

where $\boldsymbol{p}$ is the vector of the lattice position $\{(IL_x, JL_y, KL_z), (I, J, K) \in \mathbb{Z}\}$, (L_x, L_y, L_z) are the dimensions of the lattice, and the prime sign beside the second summation indicates that $i = j$ is excluded when $\boldsymbol{p} = 0$. The long-range nature of $\boldsymbol{G}$ precludes a choice of short cut-off distance and makes the direct summation cumbersome $[O(N^2)]$. Ewald summation, originally introduced to calculate Coulombic interactions, is a standard technique of treating long-range interactions in periodic boundary conditions by splitting a *periodic* $\boldsymbol{G}$ into a short-range part that converges quickly in real space and a long-range part that converges quickly in wave space. After the application of Ewald summation by Beenakker's decomposition [50], the magnetic field [Eq. (7)] is decomposed into three superposable parts, a self part $\boldsymbol{B}^{\infty,0}$, a real-space part $\boldsymbol{B}^{\infty,r}$, and a wave-space part $\boldsymbol{B}^{\infty,k}$, such that

$$\boldsymbol{B}^{\infty,0} = \left(\frac{\mu_0}{4\pi a^3 \chi} - \frac{\mu_0 \alpha^3}{3\pi^{3/2}}\right)\boldsymbol{m}_i(\boldsymbol{x}_i), \tag{8a}$$

$$\boldsymbol{B}^{\infty,r} = -\frac{\mu_0}{4\pi}\sum_{\boldsymbol{p}}\sum_{j=1}^{N}\left[\left(\frac{3\boldsymbol{y}\boldsymbol{y}}{r^5} - \frac{\boldsymbol{I}}{r^3}\right)\mathrm{erfc}(\alpha r)\right.$$
$$\left. + \left(\frac{3\boldsymbol{y}\boldsymbol{y}}{r^4} - \frac{\boldsymbol{I}}{r^2} + 2\alpha^2\frac{\boldsymbol{y}\boldsymbol{y}}{r^2}\right)\frac{2\xi}{\sqrt{\pi}}e^{-\alpha^2 r^2}\right]\cdot\boldsymbol{m}_j(\boldsymbol{x}_j), \tag{8b}$$

$$\boldsymbol{B}^{\infty,k} = \frac{\mu_0}{\Omega}\sum_{\boldsymbol{k}\neq 0}e^{-\mathrm{i}\boldsymbol{k}\cdot\boldsymbol{x}_i}e^{-\frac{k^2}{4\alpha^2}}\frac{\boldsymbol{k}\boldsymbol{k}}{k^2}\cdot\sum_{j=1}^{N}e^{\mathrm{i}\boldsymbol{k}\cdot\boldsymbol{x}_j}\boldsymbol{m}_j(\boldsymbol{x}_j), \tag{8c}$$

where Ω is the volume of the lattice, $\boldsymbol{k}$ is the wave vector $\{(2I\pi/L_x, 2J\pi/L_y, 2K\pi/L_z), (I, J, K) \in \mathbb{Z}\}$, $\boldsymbol{y} = \boldsymbol{x}_i - \boldsymbol{x}_j + \boldsymbol{p}$, $r = |\boldsymbol{y}|$, and α is the Ewald splitting parameter [45]. The details of the derivation of Eq. (8) can be found in Appendix A.

The real-space part, $\boldsymbol{B}^{\infty,r}$, decays exponentially in the real space as shown in Eq. (8). A cut-off radius r_c therefore can be chosen, and the associated cut-off error ε_r is calculated as $\varepsilon_r \sim e^{-\alpha^2 r_c^2}$. Similarly, the wave-space part, $\boldsymbol{B}^{\infty,k}$, also decays exponentially in the wave space, as shown in Eq. (8c). Thus, a cut-off wave number k_c can be chosen, and the associated cut-off error ε_k is calculated as $\varepsilon_k \sim e^{-k_c^2/4\alpha^2}$.

The value of α can be chosen arbitrarily, and the overall result is independent of α, but α plays a significant role in determining the computational load of each part. If α is chosen large, a particle only interacts with a few neighboring particles, and the computational complexity of the real space scales as $O(N)$. The particle-mesh technique implements this strategy to ease the computational load

in the real-space sum while at the expense of the wave-space sum. This strategy is feasible because a Fourier transform, $\sum_{j=1}^{N} e^{-i\mathbf{k}\cdot\mathbf{x}_j}$, and an inverse Fourier transform, $\sum_{\mathbf{k}\neq 0} e^{i\mathbf{k}\cdot\mathbf{x}_i}$, are embedded in the wave-space sum. Fast Fourier transform (FFT) can be applied to calculate the wave-space sum, and the computational complexity can be reduced to $O(N \log N)$. However, since FFT requires a regularized mesh grid, and the center of the particles do not necessarily coincide with grid points, some care needs to be taken before a direct implementation of FFT. The particle-mesh technique utilizes an interpolation algorithm to represent the particles by regularized mesh grids. Lagrangian interpolation is used in PME [46], B-spline interpolation is used in SPME [48], and a Gaussian kernel is used in SE [45], which is implemented in this study and is discussed below.

A splitting parameter θ is introduced into the wave coefficient of the wave-space sum, such that

$$e^{-\frac{k^2}{4\alpha^2}} = e^{-\frac{\theta k^2}{8\alpha^2}} e^{-\frac{(1-\theta)k^2}{4\alpha^2}} e^{-\frac{\theta k^2}{8\alpha^2}}. \tag{9}$$

Substituting this wave coefficient back into the wave-space sum yields

$$\mathbf{B}^{\infty,k} = \frac{\mu_0}{\Omega} \sum_{\mathbf{k}\neq 0} e^{\frac{\theta k^2}{8\alpha^2}} e^{-i\mathbf{k}\cdot\mathbf{x}_i} e^{-\frac{(1-\theta)k^2}{4\alpha^2}} \frac{\mathbf{k}\mathbf{k}}{k^2} \cdot \widehat{\mathbf{H}}(\mathbf{k}), \tag{10}$$

where

$$\widehat{\mathbf{H}}(\mathbf{k}) = \sum_{j=1}^{N} e^{-\frac{\theta k^2}{8\alpha^2}} e^{i\mathbf{k}\cdot\mathbf{x}_j} \mathbf{m}_j, \tag{11}$$

which is the distribution function in Fourier space, and it is the Fourier transform of $\mathbf{H}(\mathbf{x})$. Note that $\exp[-\theta k^2/(8\alpha^2)]$ is the Fourier transform of $[2\alpha^2/(\pi\theta)]^{2/3} \exp(-2\alpha^2 r^2/\theta)$, and $\exp(i\mathbf{k}\cdot\mathbf{x}_j)$ is the Fourier transform of $\delta(\mathbf{x}-\mathbf{x}_j)$. By the convolution theorem, $\mathbf{H}(\mathbf{x})$ can be calculated by an inverse Fourier transform that

$$\mathbf{H}(\mathbf{x}) = \sum_{j=1}^{N} \left(\frac{2\alpha^2}{\pi\theta}\right)^{3/2} e^{-\frac{2\alpha^2|\mathbf{x}-\mathbf{x}_j|}{\theta}} \mathbf{m}_j(\mathbf{x}_j), \tag{12}$$

which is the distribution function that distributes a dipole $\mathbf{m}_j$ at $\mathbf{x}_j$ to the adjacent grid points at $\mathbf{x}$ with a Gaussian kernel. A scaled distribution function in Fourier space is defined as

$$\widehat{\widetilde{\mathbf{H}}}(\mathbf{k}) \equiv e^{-\frac{(1-\theta)k^2}{4\alpha^2}} \frac{\mathbf{k}\mathbf{k}}{k^2} \cdot \widehat{\mathbf{H}}(\mathbf{k}), \tag{13}$$

which is the Fourier transform $\widetilde{\mathbf{H}}(\mathbf{x})$. The wave-space field becomes

$$\mathbf{B}^{\infty,k} = \frac{\mu_0}{\Omega} \sum_{\mathbf{k}\neq 0} e^{-\frac{\theta k^2}{8\alpha^2}} e^{-i\mathbf{k}\cdot\mathbf{x}_i} \widehat{\widetilde{\mathbf{H}}}(\mathbf{k}). \tag{14}$$

The wave-space field is evaluated by applying the convolution theorem again, becoming

$$\mathbf{B}^{\infty,k} = \mu_0 \int \widetilde{\mathbf{H}}(\mathbf{x}) \left(\frac{2\alpha^2}{\pi\theta}\right)^{3/2} e^{-\frac{2\alpha^2|\mathbf{x}_i-\mathbf{x}|^2}{\theta}} d\mathbf{x}. \tag{15}$$

The integration can be completed by utilizing trapezoidal quadrature. This last step is the interpolation of $\widetilde{\mathbf{H}}(\mathbf{x})$ from grid points to the center of the particle. Note that the dipole of the particle is distributed to a number of grid points that are closest to the center of the particle and that the distance between a grid point and the center of the particle $|\mathbf{x}-\mathbf{x}_i|$ is evaluated as the minimum image distance.

Two sources of errors exist in evaluating the wave-space sum. One source of error is associated with the cut-off wave number k_c that determines the number of grid points in each direction of the simulation box. The resolution of discretization dictates the accuracy of the FFT. The other

source of error is associated with the distribution [Eq. (12)] or interpolation [Eq. (15)]. This error is determined by the number of grid points, P, that are chosen for distribution. An implementation of a standard FFT algorithm (FFTW package in this study) with a sufficient discretization resolution can generate an accuracy at machine precision. Thus, the Gaussian kernel in distribution or interpolation depends exclusively on the value of P, and the minimum wave space error scales as $e^{-P\pi/2}$ [45]. Since it is exponentially decaying, the accuracy of the SE method increases rapidly by including a larger value of P.

After the dipoles are evaluated, the total potential energy is [29]

$$U = -\frac{1}{2}\sum_i \boldsymbol{m}_i \cdot \boldsymbol{B}^\infty = -\frac{1}{2}\sum_{j,k}(\boldsymbol{\Phi}^\infty)_{jk}^{-1} : \boldsymbol{B}_j^\infty \boldsymbol{B}_k^\infty, \tag{16}$$

and the magnetic force on particle i is

$$\boldsymbol{F}_i^{\mathrm{M}} = -\nabla_{\boldsymbol{x}_i} U = \frac{1}{2}\sum_{j,k}\nabla_{\boldsymbol{x}_i}(\boldsymbol{\Phi}^\infty)_{jk}^{-1} : \boldsymbol{B}_j^\infty \boldsymbol{B}_k^\infty. \tag{17}$$

The following property is applied to evaluate the gradient of a matrix inverse [29],

$$\nabla_{\boldsymbol{x}_i}(\boldsymbol{\Phi}^\infty)^{-1} = -(\nabla_{\boldsymbol{x}_i}\boldsymbol{\Phi}^\infty) : (\boldsymbol{\Phi}^\infty)^{-1}(\boldsymbol{\Phi}^\infty)^{-1}. \tag{18}$$

Thus, the magnetic force of particle i becomes

$$\boldsymbol{F}_i^{\mathrm{M}} = -\frac{1}{2}\sum_{j,k}(\nabla_{\boldsymbol{x}_i}\boldsymbol{\Phi}^\infty)_{jk} : \boldsymbol{m}_j \boldsymbol{m}_k. \tag{19}$$

Once the dipoles of particles are obtained, the magnetic force of each particle can be calculated by Eq. (19). A benchmark of the calculation of the dipole using the aforementioned method is shown in Appendix C.

III. STOKESIAN DYNAMICS AND DYNAMIC SYSTEM

At the low limit of Reynolds number (Re $\to$ 0), which is the assumption of this work due to the small size of the particles, the disturbance velocity $\boldsymbol{u}'$ is a solution to the Stokes' equation, and it can be expressed as an expansion of multipoles (analogous to the magnetic problem) such that

$$\boldsymbol{u}'(\boldsymbol{x}) = \frac{1}{8\pi\eta_0}\sum_{i=1}^N\left[\left(1+\frac{a^2}{6}\nabla^2\right)\boldsymbol{J}(\boldsymbol{x}-\boldsymbol{x}_i)\cdot\boldsymbol{F}_i^{\mathrm{H}} - \left(1+\frac{a^2}{10}\nabla^2\right)\nabla\boldsymbol{J}(\boldsymbol{x}-\boldsymbol{x}_i):\boldsymbol{D}_i^{\mathrm{H}}+\cdots\right], \tag{20}$$

where η_0 is the viscosity of the solvent, $\boldsymbol{F}_i^{\mathrm{H}}$ is the hydrodynamic force of particle i that is located at position $\boldsymbol{x}_i$, $\boldsymbol{D}_i^{\mathrm{H}}$ is the hydrodynamic force dipole of particle i that includes an antisymmetric component, torque, $\boldsymbol{T}_i^{\mathrm{H}}$, a symmetric component, stresslet, $\boldsymbol{S}_i^{\mathrm{H}}$, and an isotropic component, and $\boldsymbol{J}(\boldsymbol{x}-\boldsymbol{x}_i)$ is the stokeslet such that

$$\boldsymbol{J}(\boldsymbol{x}-\boldsymbol{x}_i) = \frac{(\boldsymbol{x}-\boldsymbol{x}_i)(\boldsymbol{x}-\boldsymbol{x}_i)}{|\boldsymbol{x}-\boldsymbol{x}_i|^3} + \frac{\boldsymbol{I}}{|\boldsymbol{x}-\boldsymbol{x}_i|}. \tag{21}$$

In this study and many other studies, the multipole is truncated at dipole level, except for the isotropic components of the quadrupole and octupole [33,51]. The hydrodynamic forces and forcedipoles of the particles can be directly related to the velocities and the velocitygradients of the particles by using Faxén formulas [52], such that

$$\boldsymbol{U}^\infty - \boldsymbol{U}_i = \frac{\boldsymbol{F}_i^{\mathrm{H}}}{6\pi\eta_0 a} + \left(1+\frac{a^2}{6}\nabla^2\right)\boldsymbol{u}_i', \tag{22a}$$

$$\boldsymbol{\Omega}^\infty - \boldsymbol{\Omega}_i = \frac{\boldsymbol{T}_i^{\mathrm{H}}}{8\pi\eta_0 a^3} + \frac{1}{2}\nabla\times\boldsymbol{u}_i', \tag{22b}$$

$$E^{\infty} - E_i = \frac{S_i^{\mathrm{H}}}{\frac{20}{3}\pi\,\eta_0 a^3} + \left(1 + \frac{a^2}{10}\nabla^2\right)\frac{1}{2}\left(\nabla u_i' + (\nabla u_i')^T\right), \tag{22c}$$

where U^{∞}, $\mathbf{\Omega}^{\infty}$, and E^{∞} are the translational velocity, angular velocity, and rate of strain of an imposed flow, respectively; U_i, $\mathbf{\Omega}_i$, and E_i are the translational velocity, angular velocity, and rate of strain of the particle, respectively; and T_i^{H} and S_i^{H} are the hydrodynamic torque and stresslet of the particle, respectively. The torque and the stresslet are the antisymmetric and the symmetric component of the force-dipole D^{H}, respectively. Note that E_i is zero for a rigid particle. By combining Eq. (20) and Eq. (22), a linear system can be written as

$$\begin{bmatrix} \mathcal{U}^{\mathrm{H}} \\ E^{\infty} \end{bmatrix} = \mathcal{M}^{\infty} \cdot \begin{bmatrix} \mathcal{F}^{\mathrm{H}} \\ S^{\mathrm{H}} \end{bmatrix}, \tag{23}$$

where $\mathcal{U}^{\mathrm{H}} = [U^{\infty} - U_i, \mathbf{\Omega}^{\infty} - \mathbf{\Omega}_i]^T$, $\mathcal{F}^{\mathrm{H}} = [F^{\mathrm{H}}, T^{\mathrm{H}}]^T$, and $\mathcal{M}^{\infty}$ is called mobility tensor. The infinity sign is introduced on the superscript because particles are treated as point particles, and $\mathcal{M}^{\infty}$ captures the far-field interactions. In Stokesian dynamics, near-field interactions are added in a pair-wise fashion to the far-field interactions to construct a grand resistance tensor $\mathcal{R}$, such that

$$\mathcal{R} = (\mathcal{M}^{\infty})^{-1} + R_{2\mathrm{B}} - R_{2\mathrm{B}}^{\infty}, \tag{24}$$

where $R_{2\mathrm{B}}$ is obtained by solving a two-particle system, and an exact solution exists for a two-sphere problem [53]. The two-body far-field part $R_{2\mathrm{B}}^{\infty}$ is subtracted to avoid double counting, as it is already included in $(\mathcal{M}^{\infty})^{-1}$. The difference $(R_{2\mathrm{B}} - R_{2\mathrm{B}}^{\infty})$ is also known as the lubrication interaction. As mentioned before, $\mathcal{R}$ captures the far-field many-body interactions with a correction of near-field interactions. The hydrodynamic force and force-dipole can be related to the velocity and the velocity gradient, such that

$$\begin{bmatrix} \mathcal{F}^{\mathrm{H}} \\ S^{\mathrm{H}} \end{bmatrix} = \mathcal{R} \cdot \begin{bmatrix} \mathcal{U}^{\mathrm{H}} \\ E^{\infty} \end{bmatrix}, \tag{25}$$

where the grand resistance tensor $\mathcal{R}$ is made of four submatrices, such that

$$\mathcal{R} = \begin{bmatrix} R_{\mathrm{FU}} & R_{\mathrm{FE}} \\ R_{\mathrm{SU}} & R_{\mathrm{SE}} \end{bmatrix}, \tag{26}$$

where R_{FU} relates force to velocity, R_{FE} relates force to rate of strain, R_{SU} relates stresslet to velocity, and R_{SE} relates stresslet to rate of strain. The linear systems of Eq. (23) and Eq. (25) can be manipulated and solved by using the Krylov subspace method. The details of the derivation can be found in the work by Swan and Brady [54].

The evaluation of $(R_{2\mathrm{B}} - R_{2\mathrm{B}}^{\infty})$ scales as $O(N)$, since a cut-off radius can be chosen for this near-field interaction. The evaluation of the far-field interaction $\mathcal{M}^{\infty}$ follows the same strategy that is applied in evaluating $\mathbf{\Phi}^{\infty}$ in magnetics by using a *periodic stokeslet* [50,55]. The periodic stokeslet is split into two parts: a real-space part that converges exponentially in real space and a wave space part that is evaluated by using SE [43]. Benchmarks of calculations of hydrodynamic interactions are shown in Appendix C.

After Eq. (25) is formulated, a balance between the magnetic and hydrodynamics can be built, such that

$$F^{\mathrm{H}} + F^{\mathrm{M}} = 0. \tag{27}$$

Note that Brownian effects are neglected in this study. The velocity of a particle is then calculated to be

$$U = R_{\mathrm{FU}}^{-1} \cdot (F^{\mathrm{M}} + R_{\mathrm{FE}} : E^{\infty}) + U^{\infty}, \tag{28}$$

where R_{FU} is a submatrix of $\mathcal{R}$ that relates force to velocity, and R_{FE} relates force to rate of strain.

Suppose that particles are suspended in a fluid upon which a shear flow, $U^\infty = (\dot{\gamma}y, 0, 0)$, is imposed. The hydrodynamic force scales as $6\pi\eta_0 a^2\dot{\gamma}$, and the magnetic force scales as $\chi^2 V^2 B^2/(\mu_0 a^4)$, where B is the magnitude of the magnetic field. Taking the ratio between the hydrodynamic force and magnetic force gives a dimensionless parameter,

$$\text{Ma} = \frac{27\eta_0\dot{\gamma}\mu_0}{8\pi\chi^2 B^2}, \tag{29}$$

which is the so-called *Mason* number [56]. The dynamics of the magnetic suspensions are dictated by Mason number and the direction of the magnetic field.

The total stress of the suspension is [35]

$$\Sigma = \text{I.T.} + 2\eta_0 E^\infty + \frac{1}{V}\sum_{i=1}^{N}\left(S_i^{\text{H}} + S_i^{\text{M}}\right), \tag{30}$$

where I.T. is the isotropic part, η_0 is the viscosity of the suspending medium, S^{H} and S^{M} are the hydrodynamic stresslet and "elastic" stress due to the interparticle forces F^{M} [57], respectively, and they are given as

$$S^{\text{H}} = R_{\text{SU}} \cdot (U^\infty - U) + R_{\text{SE}} : E^\infty, \tag{31a}$$

$$S^{\text{M}} = -xF^{\text{M}}. \tag{31b}$$

Finally, the relative viscosity is calculated to be

$$\frac{\eta}{\eta_0} = 1 + \frac{1}{\eta_0\dot{\gamma}}\frac{1}{V}\sum_{i=1}^{N}\left(S_i^{\text{H}} + S_i^{\text{M}}\right)_{yx}, \tag{32}$$

where the yx component of the hydrodynamic stresslet and the elastic stresslet are used to calculate the shear viscosity when the shear flow is imposed in the xy plane, with x being the flow direction and y being the flow-gradient direction.

IV. RESULTS AND DISCUSSION

A. Simulations of monolayer of magnetic particles in constant fields

In a simulation of a monolayer of particles, the particles are initially placed in a two-dimensional plane, and the particles remain in the plane through the simulation because of the symmetry of the magnetic and hydrodynamic interactions (no external force is imposed to constrain the particles). The interactions are still threedimensional, and a periodic cell replicates itself in the three-dimensional space to represent an unbounded infinite domain. The monolayer sheets are separated far away (a distance of 16 particle radii in this study) in the shear-flow-vorticity direction so that the effect of the separation on the viscosity can be neglected. The viscosity is calculated by taking an average over the particles, the time steps, and the initial realizations. In the constrained two-dimensional simulations, a total of 25 particles, 20 strain units, and 20 initial realizations are applied in the simulations. A constant magnetic field is applied in two directions: in the shear-flow direction, $\mathbf{b} \parallel \mathbf{u}$, or in the shear-flow-gradient direction, $\mathbf{b} \parallel \nabla\mathbf{u}$, where $\mathbf{b}$ is the dimensionless magnetic field.

When the field is applied in the shear-flow-gradient direction, particles form linear structures that are perpendicular to the flow direction [Fig. 1(a)] at first. At later times, the linear structures further interact magnetically, and a more two-dimensional structure is formed [Fig. 1(b)], of which the major axis points in the flow-gradient direction. The magnetic interactions between particles give rise to an enhanced resistance to the flow, especially as the structure percolates in the flow-gradient direction. As the Mason number decreases, i.e., an increase in the magnetic field, the structures become stronger, and the energy that is required to disturb the structure by the shear flow subsequently increases. Thus, a magnetic-thickening phenomenon with decreasing Mason number
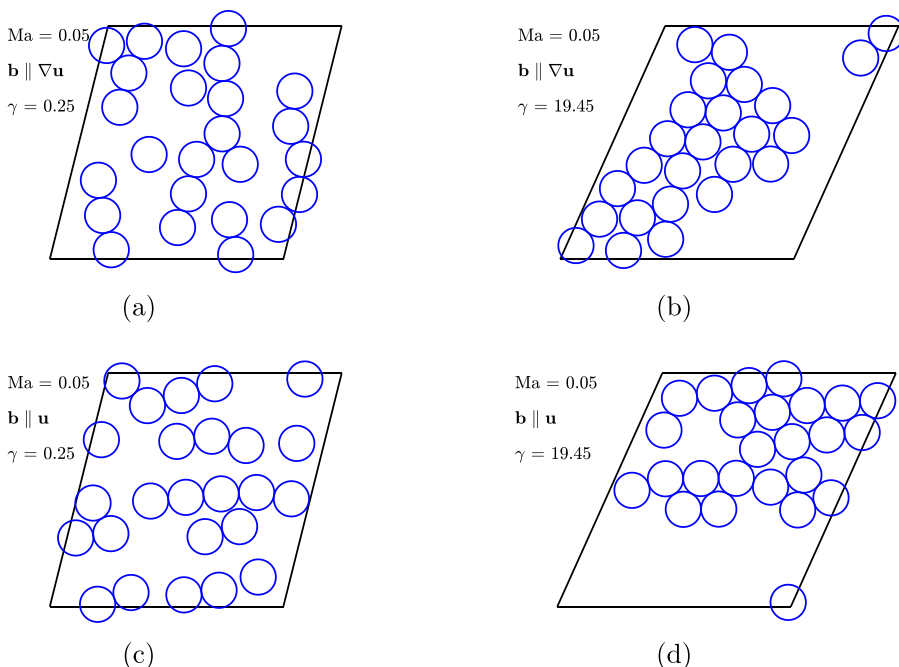
FIG. 1. Snapshots of the configurations at strain units $\gamma = 0.25$ and $\gamma = 3.45$ under different field directions at the area fraction of $\phi_A = 0.45$ and Mason number of Ma $= 0.05$. (a) Snapshot of the configuration at the strain unit $\gamma = 0.25$ when the field is in the shear-flow-gradient direction ($\mathbf{b} \parallel \nabla\mathbf{u}$). (b) Snapshot of the configuration at the strain unit $\gamma = 3.45$ when the field is in the shear-flow-gradient direction ($\mathbf{b} \parallel \nabla\mathbf{u}$). (c) Snapshot of the configuration at the strain unit $\gamma = 0.25$ when the field is in the shear-flow direction ($\mathbf{b} \parallel \mathbf{u}$). (d) Snapshot of the configuration at the strain unit $\gamma = 3.45$ when the field is in the shear-flow direction ($\mathbf{b} \parallel \mathbf{u}$).

is observed (the red circular symbols in Fig. 2) when the field is applied in the shear-flow-gradient direction. Although this result is reminiscent of a shear-thinning phenomenon, i.e., a decrease in the viscosity as an increase in the Mason number, we choose not to utilize this terminology, which is traditionally used to describe a reduction in viscosity that is caused by shear-induced orientation of the structured fluid in the flow direction. In this case, the decrease in viscosity results from an actual breakdown of the structure, not alignment; thus, we choose to focus on the role that increasing the magnetic body force, which is typically the case in experimentation, has on the overall rheology of the fluid.

When the field is applied in the shear-flow direction [Fig. 1(c)], particles form structures that are parallel to the flow direction. Intuitively, the formed structures will travel along the flow and slide passing each other, rendering less resistance to the flow. A magnetic-thinning phenomenon is expected to happen. However, the magnetic interactions drive the columns to further accumulate into thicker columns [Fig. 1(d)], and the accumulation happens across the shear-flow-gradient direction. Thus, a magnetic-thickening phenomenon is also observed when the field is applied in the shear-flow direction (the blue square symbols in Fig. 2).

The dependence of the relative viscosity, η_r ($\eta_r = \eta/\eta_0$), on the Mason number at different area fractions are shown in Fig. 2. The error bars in Fig. 2 reflect the difference of the viscosity because of the different initial realizations. Since the motion of the particles is decreased by one degree of freedom, a minor change in the configuration can cause a major difference in the dynamics and viscosity. At a high Mason number, when the magnetic interactions are weak, no significant structures are formed, as any formed structures are easily disrupted by the shear flow. Thus, the distribution of the particles are more isotropic, and the dependence on the initial realization is weak
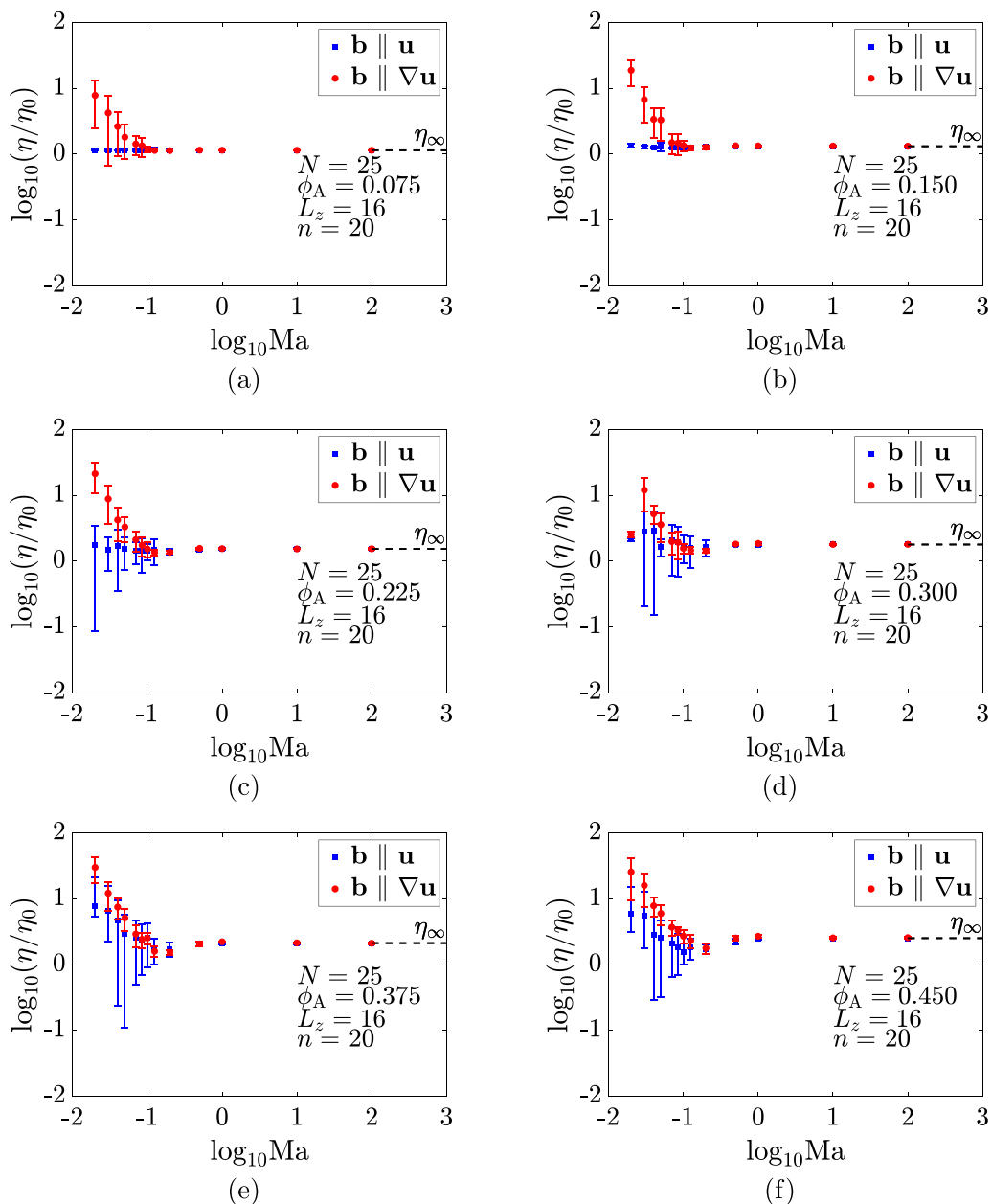
FIG. 2. The dependence of the relative viscosity on the Mason number at different area fractions, (a) 0.075, (b) 0.15, (c) 0.225, (d) 0.3, (e) 0.375, and (f) 0.45. The viscosity is averaged over the last strain unit. A constant field $\mathbf{b}$ is applied in the shear-flow direction $\mathbf{u}$ (blue square symbol) or the shear-flow-gradient direction $\nabla\mathbf{u}$ (red circle symbol).

(smaller error bars in Fig. 2 at high Ma). At a low Mason number, however, structures are formed, and the dependence on the initial realization is more pronounced. A variation in the initial realization can cause a significant difference in the configuration at steady state and therefore a difference in the viscosity. As shown in Fig. 3, a simulation of 24 particles in the same initial positions with one
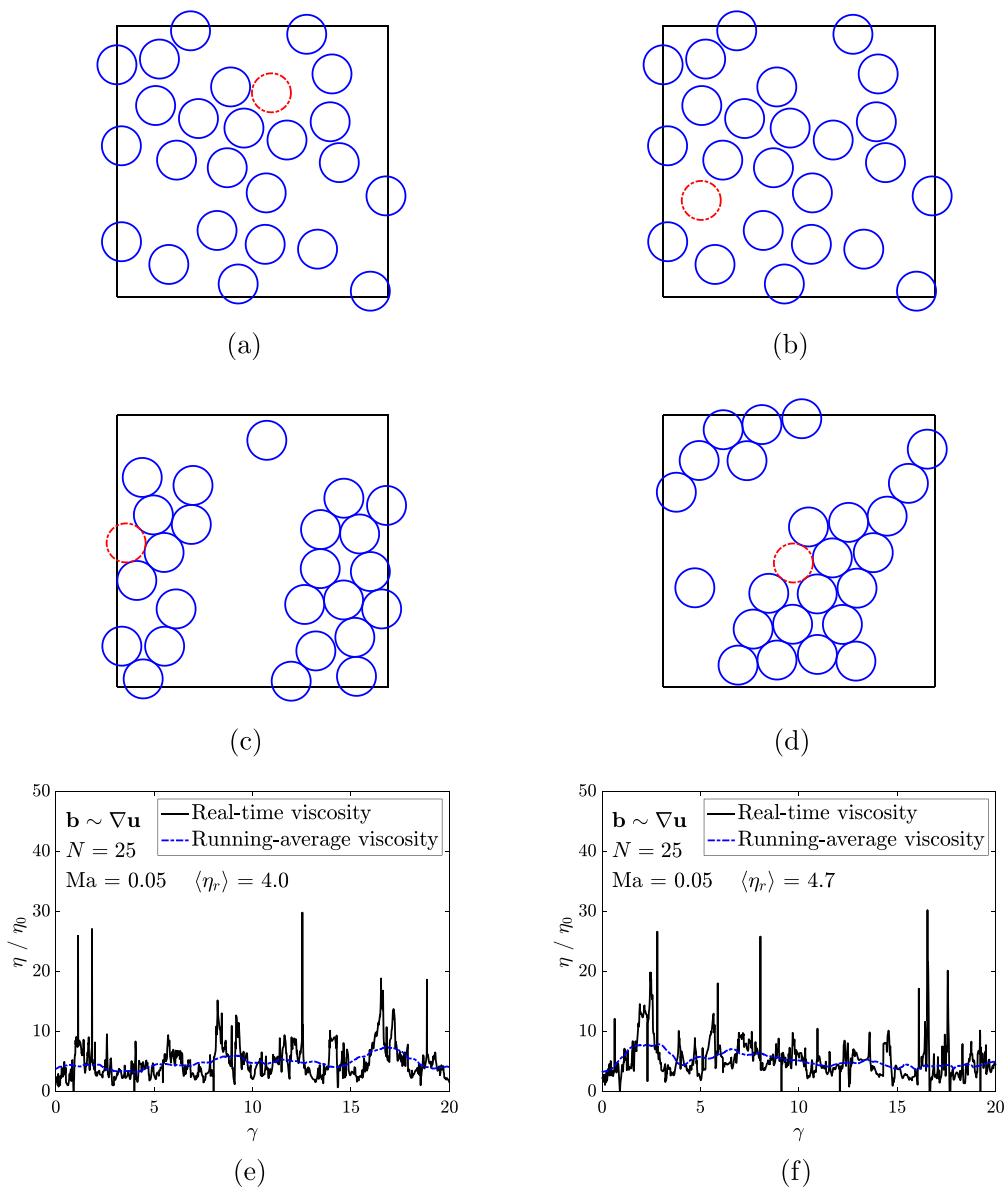
(a)

(b)

(c)

(d)

(e)

(f)

FIG. 3. A comparison of the configurations and the averaged relative viscosity with similar initial configurations. In (a) and (b), the initial positions of the 24 particles are the same (blue solid line) except 1 particle (red dash dotted line). The resulting configurations at steady state are shown in (c) and (d). The real-time viscosity and running-average viscosity are shown in (e) and (f), where the running-average viscosity is calculated by averaging over every strain unit. (a) Initial configuration No. 1. (b) Initial configuration No. 2. (c) Configuration at steady state with initial configuration No. 1. (d) Configuration at steady state with initial configuration No. 2. (e) Averaged relative viscosity that starts with the initial configuration No. 1. (f) Averaged relative viscosity that starts with the initial configuration No. 2.

particle being moved from the upper right to the lower left resulted in configurations that differ at steady state. Further, at steady state, the viscosity of configuration No. 2 [Fig. 3(f)] is more than 18% the viscosity of configuration No. 1 [Fig. 3(e)]. Therefore, cautious measures should be taken when

conducting a constrained two-dimensional simulation, especially at a high area fraction and/or a low Mason number.

B. Fully three-dimensional simulations of magnetic particles in constant fields

After the two-dimensional constraint is removed, the dynamics of the particles that are suspended in a fully three-dimensional space are simulated. In most cases, 216 particles are included in a cubic simulation cell at various volume fractions (from 0.05 to 0.30). As an additional dimension is exploited, an additional magnetic field can be applied in the shear-flow-vorticity direction, i.e., $\mathbf{b} \parallel \nabla \times \mathbf{u}$.

The dependence of the relative viscosity on the Mason number at different volume fractions are shown in Fig. 4. At lower volume fractions [Figs. 4(a) and 4(b)], the magnetic interactions are feeble, as the separations between the particles are large, and the effects of the magnetic interactions are therefore insignificant or modest. When the field is in the shear-flow-gradient direction, a modest magnetic-thickening phenomenon is seen, while the dependence on the Mason number is trivial when the field is in the shear-flow direction or the shear-flow-vorticity direction. At higher volume fractions, the strength of the magnetic interactions increases. Appreciable magnetic-thickening phenomena are observed when the field is in the shear-flow-gradient direction ($\mathbf{b} \parallel \nabla \mathbf{u}$, red circular symbols in Fig. 4), which is similar to the constrained two-dimensional case. When the field is in the shear-flow-vorticity direction ($\mathbf{b} \parallel \nabla \times \mathbf{u}$), linear structures are formed that are perpendicular to the plane of the shear flow and shear flow gradient. The columnar structures roll and translate along with the shear flow like rolling rods. At a low Mason number, the strong magnetic interactions generate fewer columnar structures with larger radial dimension, as shown in Fig. 5(a), where 1 cluster was formed, while at a high Mason number, the weak magnetic interactions generate more columnar structures with smaller radial dimension, as shown in Fig. 5(b), where 70 clusters were formed. The resistance to the flow is larger when the fluid needs to flow around more smaller objects rather than around a larger object under the same total volume condition. Therefore, under this circumstance, a magnetic-thinning phenomenon is observed, as shown by the black triangular symbols in Fig. 4. When the field is in the flow direction ($\mathbf{b} \sim \mathbf{u}$), a magnetic-thinning phenomenon is observed in the fully three-dimensional simulation, which is inconsistent to the magnetic-thickening phenomenon in the constrained two-dimensional case. In the constrained two-dimensional simulations, since the particles are only free to move in two dimensions, the columnar structures can only expand in the flow-gradient direction, which cause more resistance because of the relative motion across the flow-gradient direction. As shown in Fig. 1(d), the structure expands in the flow-gradient direction that occupies half of that dimension. On the other hand, in the fully three-dimensional simulations, the columnar structures can expand in both the flow-gradient direction and the flow-vorticity direction [Figs. 5(c) and 5(d)]. The clustered particles in the flow-vorticity directions do not have relative motions; thus, they have no lubrication interactions. Similar to the case where the field is in the flow-vorticity direction, at a smaller Mason number, fewer larger structures are formed [Fig. 1(c)], and at a larger Mason number, more smaller structures are formed, as shown in Fig. 5(d), where 58 clusters were formed. Moreover, the difference in the size of the error bars between Figs. 2 and 4 should be noted, which is again the result from the difference in the degrees of freedom in the movement. As the Mason number approaches infinity, the viscosity of the three field directions converge to a single value, of which the magnetic field is turned off. This single value (η_∞) can be obtained theoretically by calculating a random suspension of force-free particles under a shear flow with different volume fractions, which is benchmarked by the work of Sierou and Brady [41] (see Appendix C, Fig. 10).

The green dash dotted lines in Fig. 4 draw the boundaries to the left at values of Ma $= 0.05$ to which the results have larger numerical errors, as at a low Mason number, the percolation of particles across the simulation cell becomes noticeable. A small ratio between the dimension of the simulation cell and the characteristic length scale of the columnar structure can introduce unwanted artifacts that reduce the accuracy of the results. For instance, in Figs. 4(b) to 4(d), when the field
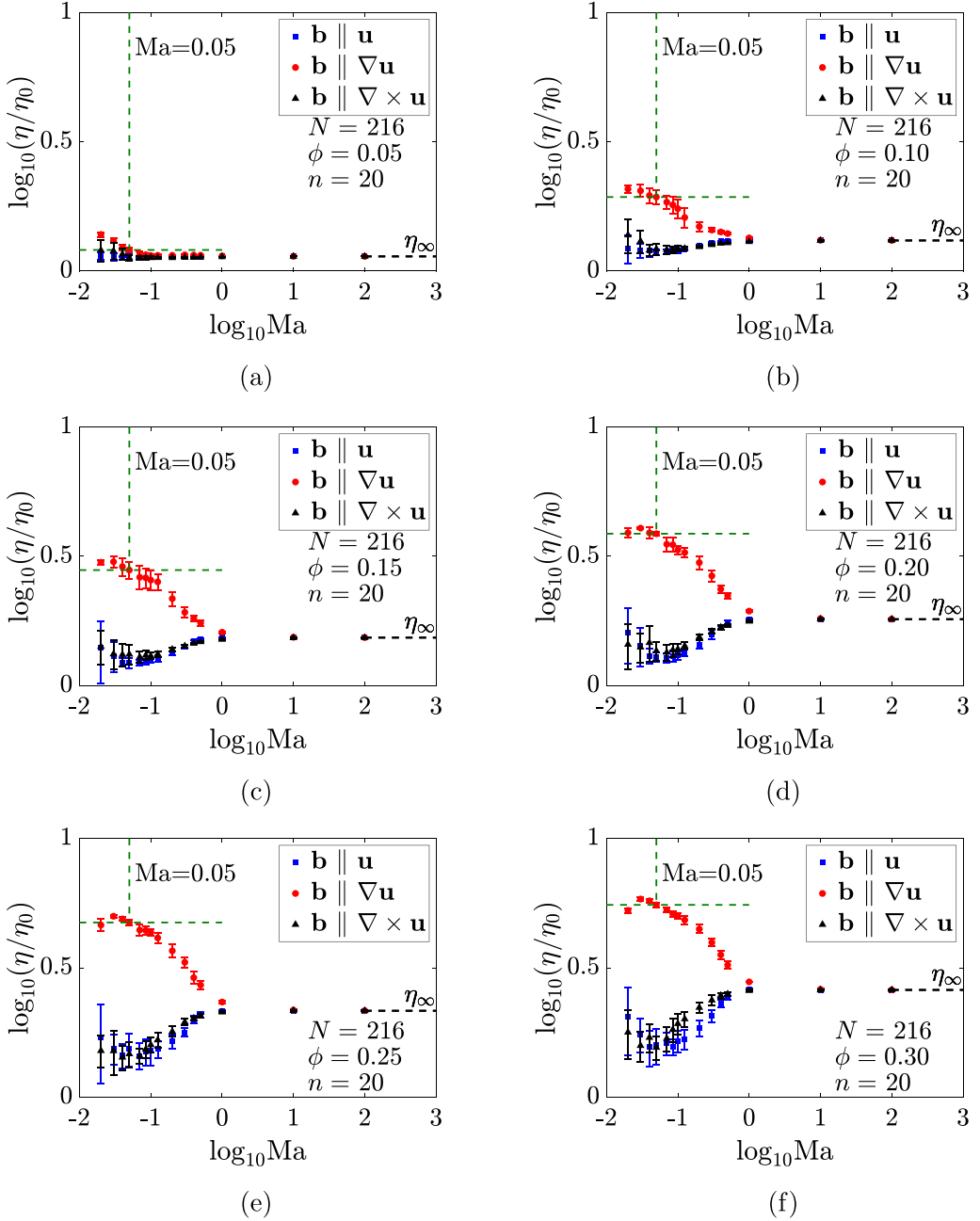
FIG. 4. The dependence of the relative viscosity on the Mason number at different volume fractions, (a) 0.05, (b) 0.10, (c) 0.15, (d) 0.20, (e) 0.25, and (f) 0.30. The viscosity is averaged over the last strain unit. A constant field **b** is applied in the shear-flow direction **u** (blue square symbol), the shear-flow-gradient direction ∇**u** (red circular symbol), or the shear-flow-vorticity direction $\nabla \times$ **u** (black triangular symbol).
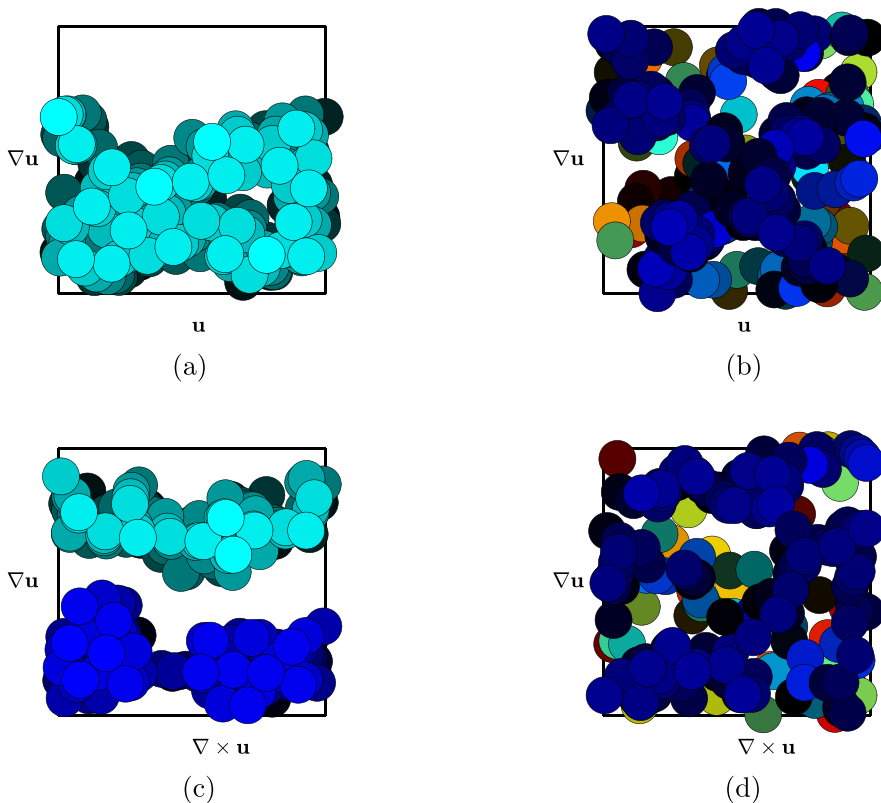
FIG. 5. Snapshots of configurations at $\gamma = 20$ at volume fraction $\phi = 0.3$ and Mason number Ma = 0.05 [(a) and (c)] and Ma = 0.5 [(b) and (d)], and the field in the flow-vorticity direction [$\mathbf{b} \parallel \nabla \times \mathbf{u}$, (a) and (b)] and in the flow direction [$\mathbf{b} \parallel \mathbf{u}$, (c) and (d)]. The magnetic field points in the direction that is perpendicular to the plane of the view, and columnar structures are formed along the direction that is perpendicular to the plane of the view. The particles in the same cluster are labeled in the same color, and the color shade indicates the depth of the particles in the plane of view. (a) The snapshot of 1 cluster that is formed (Ma = 0.05, $\mathbf{b} \parallel \nabla \times \mathbf{u}$, $\gamma = 20$). (b) The snapshot of 70 clusters that is formed (Ma = 0.5, $\mathbf{b} \parallel \nabla \times \mathbf{u}$, $\gamma = 20$). (c) The snapshot of 2 clusters that is formed (Ma = 0.05, $\mathbf{b} \parallel \mathbf{u}$, $\gamma = 20$). (d) The snapshot of 58 cluster that is formed (Ma = 0.5, $\mathbf{b} \parallel \mathbf{u}$, $\gamma = 20$).

is in the flow-gradient direction, the viscosity at Ma = 0.02 is expected to be larger than, not equal to or less than, the viscosity at Ma = 0.03. The same observation can be made from the field in the flow and flow-vorticity directions. A resolution is to increase the dimension of the simulation cell by including more particles. In Fig. 6, the dependence of the viscosity on the Mason number with different numbers of particles (keeping the same volume fraction value) is plotted. The viscosity is normalized by the high-Mason-number viscosity, η_∞. The number of the particles is increased sequentially from $N = 108$ to $N = 864$. When the dimension of the simulation cell is increased, the numerical error at low Mason number is correspondingly improved when the fields are in the shear-flow and shear-flow-vorticity directions.

In a suspension of force-free particles at the dilute limit, Einstein [58] made a correction to the viscosity of the suspension, such that $\eta/\eta_0 = 1 + 2.5\phi$, where ϕ is the volume fraction. Later, Batchelor [57] made a second-order correction to Einstein's viscosity, such that $\eta/\eta_0 = 1 + 2.5\phi + 5\phi^2$. In a suspension of particles with external forces, the scaling can be significantly different, depending on the nature and magnitude of the external force. In Fig. 7(a), the scaling between
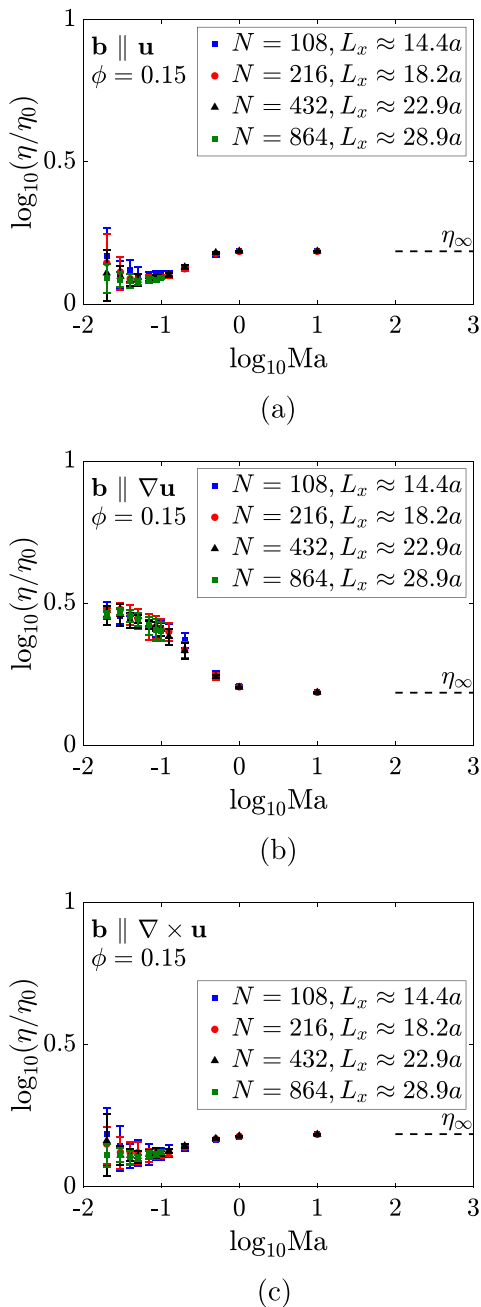
(a)

(b)

(c)

FIG. 6. A comparison of the dependence of the viscosity on the Mason number at different dimensions of the simulation cell. The volume fraction is kept at $\phi = 0.15$. The number of particles is changed from $N = 108$ to $N = 864$. (a) Shear-flow direction $\mathbf{b} \parallel \mathbf{u}$. (b) Shear-flow-gradient direction $\mathbf{b} \parallel \mathbf{u}$. (c) Shear-flow-vorticity direction $\mathbf{b} \parallel \nabla \times u$.

the relative viscosity (η/η_0) and the volume fraction (ϕ) is drawn. At low volume fraction, the relative viscosity of the suspension of magnetic particles is close to the force-free particles, which confirms the validity of the numerical results, since at low volume fraction, the magnetic interactions are not as significant, and the particles are closer to the force-free particles. The scaling shows
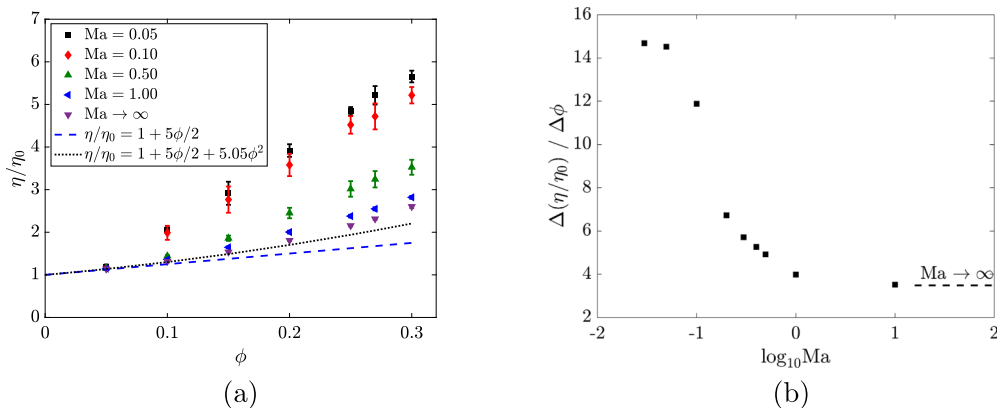
FIG. 7. The scale of the relative viscosity to the volume fraction. The blue dashed line is the Einstein's correction [58] to the viscosity at dilute limit, and the black dot dashed line is the Batchelor's correction [57] to the Einstein's viscosity. (a) Relative viscosity scaling. (b) Magnetic first-order correction.

that the viscosity is drastically increased by the introduction of the magnetic field. Figure 7(b) demonstrates the scalings of relative viscosity with respect to the volume fraction at different Mason numbers that are obtained from Fig. 7(a) when the volume fraction approaches zero. At high Mason number, the scaling approaches 2.5 (Einstein's correction), while at low Mason number, the scaling is significantly increased by the strong magnetic interactions between particles.

A comparison between the constrained two-dimensional simulation and the fully three-dimensional simulation has been made in the previous paragraphs. In Fig. 8, a direct comparison of the viscosity is drawn and the area/volume fraction is normalized by the critical area/volume fraction, ϕ_c, which is the highest possible volume fraction at the hexagonal close packing. The viscosity is normalized by the high-Mason-number-limit viscosity, η_∞. The result shows that the two types of the simulations yield different magnetic-thickening behavior when the field is in the shear-flow-gradient direction. A similar reason has been raised to explain the difference when the field is in the shear-flow direction or the shear-flow-vorticity direction. In a fully three-dimensional
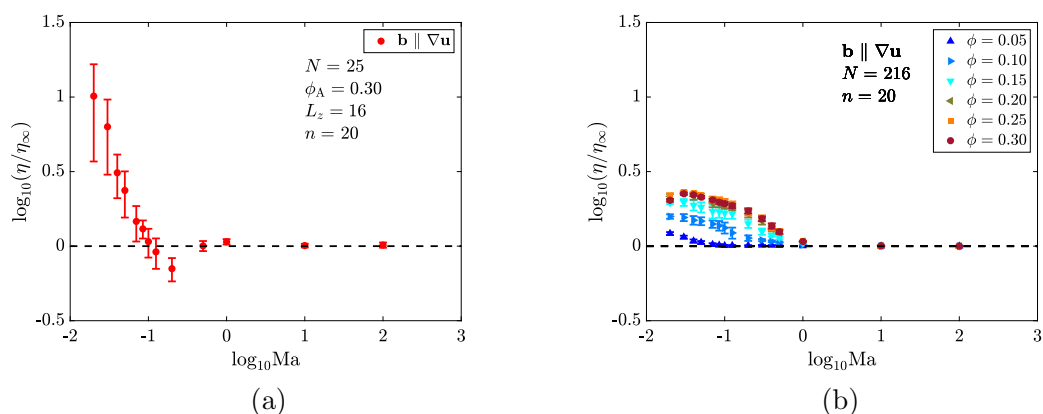

FIG. 8. A comparison of the relative viscosity between the constrained two-dimensional and the fully three-dimensional simulations. The magnetic field is in the shear-flow-gradient direction ($\mathbf{b} \parallel \nabla\mathbf{u}$). The area ($\phi_A$) or volume ($\phi$) fraction is normalized by the critical area/volume fraction at the hexagonal packing ($\phi_c^A \approx 0.91$ for areal hexagonal close packing and $\phi_c \approx 0.74$ for volumetric hexagonal close packing.) (a) Two-dimensional simulation result ($\phi_A = 0.3$, $\mathbf{b} \parallel \nabla\mathbf{u}$). (b) Three-dimensional simulation results ($\phi \in [0.05, 0.3]$, $\mathbf{b} \parallel \nabla\mathbf{u}$).

simulation, the columnar structures are free to expand in the shear-flow-vorticity direction, and no relative motion is in this direction.

V. CONCLUSION AND OUTLOOK

In this study, the dynamics and rheological properties in terms of shear viscosity are calculated from the simulations of the suspensions of particles under different constant magnetic fields by using a in-house Stokesian dynamics code.

The constrained two-dimensional and the fully three-dimensional simulations are conducted, and the results of the two types of simulations are compared. When the magnetic field is in the shear-flow-gradient direction, the magnetic-thickening phenomenon is observed in both cases. When the magnetic field is in the shear-flow-vorticity direction (only feasible in the fully three-dimensional simulation), the magnetic-thinning phenomenon is observed. When the field is in the shear-flow direction, the magnetic-thickening phenomenon is observed in the constrained two-dimensional simulation while the magnetic-thinning phenomenon is observed in the fully three-dimensional simulation. The difference is rooted in the freedom of the movement of the particles. The comparison also shows that, when the field is in shear-flow-gradient direction, the constrained two-dimensional simulation over-predicts the viscosity. The numerical robustness of the simulation method is investigated by increasing the number of particles in the simulations. Simulating the constrained two-dimensional cases should draw a caution that, since the movement of the particles miss one degree of freedom, the structures that are formed can have a notable discrepancy from the real physics. Based on the results of the fully three-dimensional simulations, a relation between the volume fraction and the relative viscosity is built at different Mason numbers. The relation grows stronger when the Mason number is smaller (stronger magnetic field), and it can provide information for predicting the viscosity of a MR fluid at a given volume fraction of the suspended particles and a Mason number.

In the future, we expect to change the properties of the magnetic fields, e.g., applying a rotating magnetic field to see the dependence of the viscosity on the frequency of the field, to include the Brownian effect in the simulation to see the dependence of the viscosity on the Péclet number, and to increase the computational capability, e.g., using GPU calculations to simulate larger systems.

ACKNOWLEDGMENTS

APPENDIX A: EWALD SUMMATION

The propagator $G(y)$ is split into two parts such that

$$G(y) = \nabla\nabla\left(\frac{1}{r}\right) = \nabla\nabla\left(\frac{\mathrm{erf}(\alpha r)}{r}\right) + \nabla\nabla\left(\frac{\mathrm{erfc}(\alpha r)}{r}\right), \tag{A1}$$

where the real-space sum, $G^r(y)$, and the wave space sum, $G^k(y)$, are given by

$$G^r(y) = \nabla\nabla\left(\frac{\mathrm{erfc}(\alpha r)}{r}\right), \tag{A2}$$

$$G^k(y) = \nabla\nabla\left(\frac{\mathrm{erf}(\alpha r)}{r}\right). \tag{A3}$$

The real-space sum can be directly obtained from the derivatives,

$$\boldsymbol{G}^r(\boldsymbol{y}) = -\left(\frac{\boldsymbol{I}}{r^3} - \frac{3\boldsymbol{y}\boldsymbol{y}}{r^5}\right)\mathrm{erfc}(\alpha r) + \left[\left(\frac{3\boldsymbol{y}\boldsymbol{y}}{r^4} - \frac{\boldsymbol{I}}{r^2}\right) + 2\alpha^2\frac{\boldsymbol{y}\boldsymbol{y}}{r^2}\right]\mathcal{E}, \tag{A4}$$

where

$$\mathcal{E} = \frac{2\alpha}{\sqrt{\pi}}\exp(-\alpha^2 r^2). \tag{A5}$$

Thus, the real-part contribution to the field is

$$\boldsymbol{B}^{\infty,r} = \boldsymbol{G}^r \cdot \boldsymbol{m}_j. \tag{A6}$$

The wave part contribution to the field is given by

$$\boldsymbol{B}^{\infty,k} = -\frac{\mu_0}{4\pi}\sum_{\boldsymbol{p}}\sum_{j=1}^{N}\boldsymbol{G}^k(\boldsymbol{y}) \cdot \boldsymbol{m}_j(\boldsymbol{x}_j). \tag{A7}$$

By Poisson's summation formula,

$$\sum_{\boldsymbol{p}}\boldsymbol{G}^k(\boldsymbol{y}) = \frac{1}{\Omega}\sum_{\boldsymbol{k}}\boldsymbol{G}^k(\boldsymbol{k}), \tag{A8}$$

where $\boldsymbol{G}^k(\boldsymbol{k})$ is calculated by the Fourier transform

$$\boldsymbol{G}^k(\boldsymbol{k}) = \int e^{\mathrm{i}\boldsymbol{k}\cdot\boldsymbol{y}}\boldsymbol{G}^k(\boldsymbol{y})d\boldsymbol{y}. \tag{A9}$$

Thus, the wave part becomes

$$\boldsymbol{B}^{\infty,k} = -\frac{\mu_0}{4\pi}\frac{1}{\Omega}\sum_{\boldsymbol{k}\neq 0}\sum_{j=1}^{N}e^{-\mathrm{i}\boldsymbol{k}\cdot(\boldsymbol{x}_i-\boldsymbol{x}_j)}\boldsymbol{G}^k(\boldsymbol{k}) \cdot \boldsymbol{m}_j(\boldsymbol{x}_j). \tag{A10}$$

The evaluation of $\boldsymbol{G}^k(\boldsymbol{k})$ becomes

$$\begin{aligned}\boldsymbol{G}^k(\boldsymbol{k}) &= \int e^{\mathrm{i}\boldsymbol{k}\cdot\boldsymbol{y}}\nabla\nabla\left(\frac{\mathrm{erf}(\alpha r)}{r}\right)d\boldsymbol{y}\\ &= -\boldsymbol{k}_i\boldsymbol{k}_j\int e^{\mathrm{i}\boldsymbol{k}\cdot\boldsymbol{y}}\frac{\mathrm{erf}(\alpha r)}{r}d\boldsymbol{y}\\ &= -\boldsymbol{k}_i\boldsymbol{k}_j\int_0^{\infty}\left[4\pi r^2\frac{\sin(kr)\mathrm{erf}(\alpha r)}{kr^2}\right]dr\\ &= -4\pi\frac{\boldsymbol{k}_i\boldsymbol{k}_j}{k^2}e^{-\frac{k^2}{4\alpha^2}}.\end{aligned} \tag{A11}$$

The wave part of magnetic field is therefore

$$\boldsymbol{B}^{\infty,k} = \frac{\mu_0}{\Omega}\sum_{\boldsymbol{k}\neq 0}\sum_{j=1}^{N}e^{-\mathrm{i}\boldsymbol{k}\cdot(\boldsymbol{x}_i-\boldsymbol{x}_j)}e^{-\frac{k^2}{4\alpha^2}}\frac{\boldsymbol{k}_i\boldsymbol{k}_j}{k^2} \cdot \boldsymbol{m}_j(\boldsymbol{x}_j). \tag{A12}$$

APPENDIX B: IMPLEMENTATION OF THE ALGORITHM

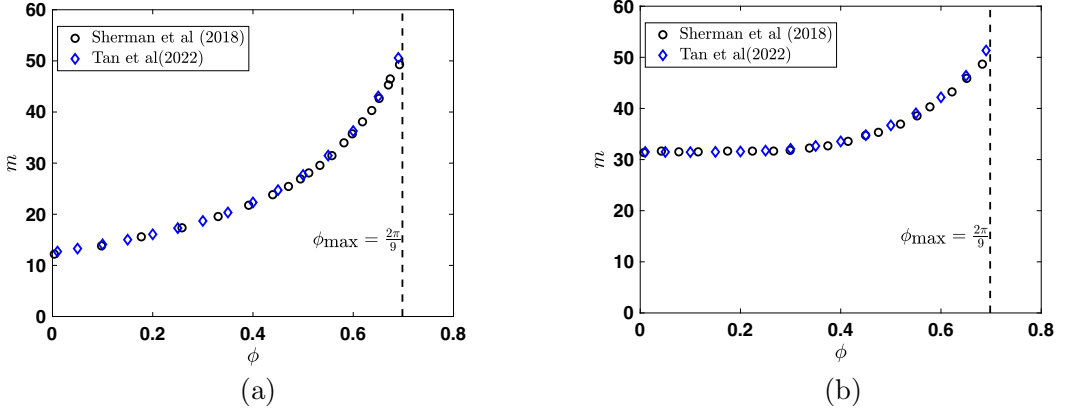The implementation of the algorithm is listed as follows.

FIG. 9. A comparison of the dipole of a BCT lattice of particles between this work and Sherman *et al.* [29]. (a) Dipole of a BCT lattice of particles at a fixed aspect ratio $L_x = L_y = (1/\sqrt{2/3})L_z$ as a function of volume fraction. (b) Dipole of a BCT lattice of particles at a fixed unit cell dimension in the field direction ($L_z = 2a$) as a function of volume fraction.

Step 1. A simulation box with dimension, L_x, L_y, and L_z ($L_z = 2a$ for mono-layer system) is generated based on the number of particles N and the volume fraction ϕ.

Step 2. An initial placement of the particles is randomly generated inside the box.

Step 3. Based on the required accuracy and the value of α, the cut-off radius r_c, the number of grid points to represent a particle, P, and the number of total grid points for FFT are obtained. The simulation box is discretized by the number of total grid points.

Step 4. The real-space part of the magnetic field, $\boldsymbol{B}^{\infty,r}$, is calculated. From the current configuration of the particles, a linked list is generated to keep track of the neighboring particles of a particular one if their separation is smaller than r_c. The real-space part, $\boldsymbol{B}^{\infty,r}$, is calculated based on Eq. (8b) for a given dipole moment $\boldsymbol{m}_i$. Note that $\boldsymbol{m}_i$ is the one that needs to be solved iteratively later.

Step 5. The wave space part of the magnetic field, $\boldsymbol{B}_k^{\infty}$, is calculated, and this procedure is decomposed into the following steps.

Step 5a. From the current configuration of the grid points, the wave value, $e^{-(1-\theta)k^2/4\alpha^2}\boldsymbol{kk}/k^2$, of each grid point is calculated.

Step 5b. For a given $\boldsymbol{m}_i$, the dipole moment $\boldsymbol{m}_i$ is distributed to grid points based on Eq. (12).

Step 5c. An FFT of $\boldsymbol{H}(\boldsymbol{x})$ that was obtained from the last step is conducted to give $\widehat{\boldsymbol{H}}(\boldsymbol{k})$.

Step 5d. The wave value that was obtained from Step 5a is multiplied by $\widehat{\boldsymbol{H}}(\boldsymbol{k})$ to give $\widehat{\widetilde{\boldsymbol{H}}}(\boldsymbol{k})$ [Eq. (13)].

Step 5e. An IFFT of $\widehat{\widetilde{\boldsymbol{H}}}(\boldsymbol{k})$ is conducted to obtain $\widetilde{\boldsymbol{H}}(\boldsymbol{x})$.

Step 5f. The magnetic fields in the wave space are interpolated from the grid points to the particles [Eq. (15)] to obtain the value of $\boldsymbol{B}_k^{\infty}$.

Step 6. Next, $\boldsymbol{B}^{\infty,r}$ and $\boldsymbol{B}_k^{\infty}$ are combined, and the self part $\boldsymbol{B}^{\infty,0}$, is added to become $\boldsymbol{B}^{\infty}$. Note that $\boldsymbol{B}^{\infty}$ is an imposed condition, so $\boldsymbol{m}_i$ is solved iteratively by using GMRES.

Step 7. The calculation of the far-field hydrodynamic interactions follow the same algorithm (Steps 4 to 6) but with Ewald summation of a different Green's function [45].

Step 8. Lubrication interactions are calculated from $\boldsymbol{R}_{2B} - \boldsymbol{R}_{2B}^{\infty}$. This calculation follows the same procedure as Step 4 but with a different cut-off radius.

Step 9. The velocity of the particles (Eq. 28) and the stresslet (Eq. 31) are calculated iteratively by using GMRES and the linear system built by Swan & Brady [54].
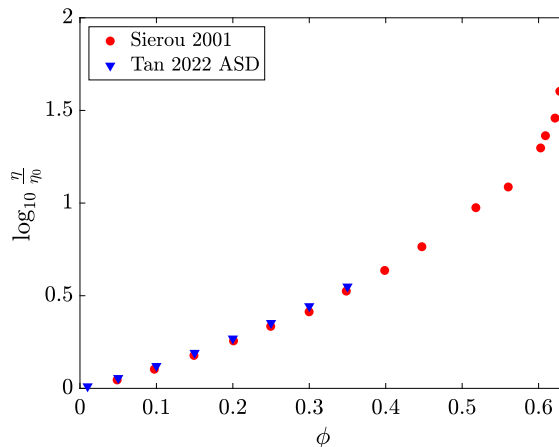
FIG. 10. A calculation of viscosity as a function of volume fraction at random distributions of spheres and a comparison with [41].

Step 10. The configuration of the particles is stepped forward in time based on the velocity that was calculated from the last step. The grid points are deformed based on the shear rate and time step size.

Steps 4 to 10 are repeated until a required strain unit is fulfilled.

APPENDIX C: BENCHMARK OF MAGNETIC CALCULATION AND HYDRODYNAMIC CALCULATION

A calculation of dipoles of body-centered tetragonal (BCT) lattice of particles with a fixed aspect ratio $\sqrt{2/3}$ [Fig. 1(a)] and fixed unit cell dimension in the field direction [Fig. 9(b)] is shown and compared with Sherman *et al.* [29].

A calculation the viscosity as a function of the volume fraction of a random suspension of force-free particles is calculated and compared with Sierou and Brady [41] as shown in Fig. 10.

[1] J. Rabinow, The magnetic fluid clutch, Electr. Eng. **67**, 1167 (1948).

[2] W. M. Winslow, Induced fibration of suspensions, J. Appl. Phys. **20**, 1137 (1949).

[3] K. D. Hermanson, S. O. Lumsdon, J. P. Williams, E. W. Kaler, and O. D. Velev, Dielectrophoretic assembly of electrically functional microwires from nanoparticle suspensions, Science **294**, 1082 (2001).

[4] K. H. Bhatt and O. D. Velev, Control and modeling of the dielectrophoretic assembly of on-chip nanoparticle wires, Langmuir **20**, 467 (2004).

[5] M. E. Leunissen, H. R. Vutukuri, and A. van Blaaderen, Directing colloidal self-assembly with biaxial electric fields, Adv. Mater. **21**, 3116 (2009).

[6] E. V. Yakovlev, K. A. Komarov, K. I. Zaytsev, N. P. Kryuchkov, K. I. Koshelev, A. K. Zotov, D. A. Shelestov, V. L. Tolstoguzov, V. N. Kurlov, A. V. Ivlev *et al.*, Tunable two-dimensional assembly of colloidal particles in rotating electric fields, Sci. Rep. **7**, 13727 (2017).

[7] S. O. Lumsdon, E. W. Kaler, and O. D. Velev, Two-dimensional crystallization of microspheres by a coplanar ac electric field, Langmuir **20**, 2108 (2004).

[8] A. Snezhko and I. S. Aranson, Magnetic manipulation of self-assembled colloidal asters, Nat. Mater. **10**, 698 (2011).

[9] A. Ahniyaz, Y. Sakamoto, and L. Bergström, Magnetic field-induced assembly of oriented superlattices from maghemite nanocubes, Proc. Natl. Acad. Sci. **104**, 17570 (2007).

[10] R. Dreyfus, J. Baudry, M. L. Roper, M. Fermigier, H. A. Stone, and J. Bibette, Microscopic artificial swimmers, Nature (London) **437**, 862 (2005).

[11] W. Gao, X. Feng, A. Pei, C. R. Kane, R. Tam, C. Hennessy, and J. Wang, Bioinspired helical microswimmers based on vascular plants, Nano Lett. **14**, 305 (2014).

[12] F. Qiu, S. Fujita, R. Mhanna, L. Zhang, B. R. Simona, and B. J. Nelson, Magnetic helical microswimmers functionalized with lipoplexes for targeted gene delivery, Adv. Funct. Mater. **25**, 1666 (2015).

[13] J. D. Jackson, *Classical Electrodynamics*, 3rd ed. (John Wiley & Sons, New York, 1999).

[14] H. J. H. Clercx and G. Bossis, Many-body electrostatic interactions in electrorheological fluids, Phys. Rev. E **48**, 2721 (1993).

[15] E. E. Keaveny and M. R. Maxey, Modeling the magnetic interactions between paramagnetic beads in magnetorheological fluids, J. Comput. Phys. **227**, 9554 (2008).

[16] D. Klingenberg, F. Van Swol, and C. Zukoski, Dynamic simulation of electrorheological suspensions, J. Chem. Phys. **91**, 7888 (1989).

[17] D. Klingenberg, F. Van Swol, and C. Zukoski, The small shear rate response of electrorheological suspensions. I. Simulation in the point–dipole limit, J. Chem. Phys. **94**, 6160 (1991).

[18] D. J. Klingenberg, C. F. Zukoski, and J. C. Hill, Kinetics of structure formation in electrorheological suspensions, J. Appl. Phys. **73**, 4644 (1993).

[19] J. E. Martin, R. A. Anderson, and C. P. Tigges, Simulation of the athermal coarsening of composites structured by a biaxial field, J. Chem. Phys. **108**, 7887 (1998).

[20] J. E. Martin, R. A. Anderson, and C. P. Tigges, Simulation of the athermal coarsening of composites structured by a uniaxial field, J. Chem. Phys. **108**, 3765 (1998).

[21] J. E. Martin, Thermal chain model of electrorheology and magnetorheology, Phys. Rev. E **63**, 011406 (2000).

[22] G. L. Gulley and R. Tao, Structures of an electrorheological fluid, Phys. Rev. E **56**, 4328 (1997).

[23] E. Climent, M. R. Maxey, and G. E. Karniadakis, Dynamics of self-assembled chaining in magnetorheological fluids, Langmuir **20**, 507 (2004).

[24] F. Smallenburg and M. Dijkstra, Phase diagram of colloidal spheres in a biaxial electric or magnetic field, J. Chem. Phys. **132**, 204508 (2010).

[25] H. G. Lagger, T. Breinlinger, J. G. Korvink, M. Moseler, A. Di Renzo, F. Di Maio, and C. Bierwisch, Influence of hydrodynamic drag model on shear stress in the simulation of magnetorheological fluids, J. Non-Newtonian Fluid Mech. **218**, 16 (2015).

[26] D. Du, D. Li, M. Thakur, and S. L. Biswal, Generating an in situ tunable interaction potential for probing 2-d colloidal phase behavior, Soft Matter **9**, 6867 (2013).

[27] A.-P. Hynninen and M. Dijkstra, Phase behavior of dipolar hard and soft spheres, Phys. Rev. E **72**, 051402 (2005).

[28] A.-P. Hynninen and M. Dijkstra, Phase Diagram of Dipolar Hard and Soft Spheres: Manipulation of Colloidal Crystal Structures by an External Field, Phys. Rev. Lett. **94**, 138303 (2005).

[29] Z. M. Sherman, D. Ghosh, and J. W. Swan, Field-directed self-assembly of mutually polarizable nanoparticles, Langmuir **34**, 7117 (2018).

[30] D. Klingenberg, F. van Swol, and C. Zukoski, The small shear rate response of electrorheological suspensions. II. Extension beyond the point–dipole limit, J. Chem. Phys. **94**, 6170 (1991).

[31] R. Bonnecaze and J. Brady, A method for determining the effective conductivity of dispersions of particles, Proc. R. Soc. London, Ser. A **430**, 285 (1990).

[32] R. Bonnecaze and J. Brady, Dynamic simulation of an electrorheological fluid, J. Chem. Phys. **96**, 2183 (1992).

[33] L. Durlofsky, J. F. Brady, and G. Bossis, Dynamic simulation of hydrodynamically interacting particles, J. Fluid Mech. **180**, 21 (1987).

[34] J. F. Brady, R. J. Phillips, J. C. Lester, and G. Bossis, Dynamic simulation of hydrodynamically interacting suspensions, J. Fluid Mech. **195**, 257 (1988).

[35] J. F. Brady and G. Bossis, Stokesian dynamics, Annu. Rev. Fluid Mech. **20**, 111 (1988).

[36] T. N. Phung, J. F. Brady, and G. Bossis, Stokesian dynamics simulation of brownian suspensions, J. Fluid Mech. **313**, 181 (1996).

[37] S. Succi, *The Lattice Boltzmann Equation: For Fluid Dynamics and Beyond* (Oxford University Press, New York, 2001).

[38] C. Pozrikidis *et al.*, *Boundary Integral and Singularity Methods for Linearized Viscous Flow* (Cambridge University Press, New York, 1992).

[39] G.-R. Liu and M. B. Liu, *Smoothed Particle Hydrodynamics: A Meshfree Particle Method* (World scientific, River Edge, 2003).

[40] Y. Saad, *Iterative Methods for Sparse Linear Systems* (SIAM, Philadelphia, 2003).

[41] A. Sierou and J. F. Brady, Accelerated stokesian dynamics simulations, J. Fluid Mech. **448**, 115 (2001).

[42] A. J. Banchio and J. F. Brady, Accelerated stokesian dynamics: Brownian motion, J. Chem. Phys. **118**, 10323 (2003).

[43] M. Wang and J. F. Brady, Spectral ewald acceleration of stokesian dynamics for polydisperse suspensions, J. Comput. Phys. **306**, 443 (2016).

[44] T. G. Kang, M. A. Hulsen, J. M. den Toonder, P. D. Anderson, and H. E. Meijer, A direct simulation method for flows with suspended paramagnetic particles, J. Comput. Phys. **227**, 4441 (2008).

[45] D. Lindbo and A.-K. Tornberg, Spectrally accurate fast summation for periodic stokes potentials, J. Comput. Phys. **229**, 8994 (2010).

[46] T. Darden, D. York, and L. Pedersen, Particle mesh ewald: An $N \cdot \log(N)$ method for ewald sums in large systems, J. Chem. Phys. **98**, 10089 (1993).

[47] R. W. Hockney and J. W. Eastwood, *Computer Simulation Using Particles* (CRC Press, Boca Raton, 1988).

[48] U. Essmann, L. Perera, M. L. Berkowitz, T. Darden, H. Lee, and L. G. Pedersen, A smooth particle mesh ewald method, J. Chem. Phys. **103**, 8577 (1995).

[49] R. E. Raab, O. L. De Lange, O. L. de Lange *et al.*, *Multipole Theory in Electromagnetism: Classical, Quantum, and Symmetry Aspects, with Applications* (Oxford University Press on Demand, New York, 2005).

[50] C. Beenakker, Ewald sum of the rotne–prager tensor, J. Chem. Phys. **85**, 1581 (1986).

[51] A. Fiore and J. Swan, Fast stokesian dynamics, J. Fluid Mech. **878**, 544 (2019).

[52] G. Batchelor and J.-T. Green, The hydrodynamic interaction of two small freely-moving spheres in a linear flow field, J. Fluid Mech. **56**, 375 (1972).

[53] D. Jeffrey and Y. Onishi, Calculation of the resistance and mobility functions for two unequal rigid spheres in low-reynolds-number flow, J. Fluid Mech. **139**, 261 (1984).

[54] J. W. Swan and J. F. Brady, The hydrodynamics of confined dispersions, J. Fluid Mech. **687**, 254 (2011).

[55] H. Hasimoto, On the periodic fundamental solutions of the stokes equations and their application to viscous flow past a cubic array of spheres, J. Fluid Mech. **5**, 317 (1959).

[56] A. P. Gast and C. F. Zukoski, Electrorheological fluids as colloidal suspensions, Adv. Colloid Interface Sci. **30**, 153 (1989).

[57] G. Batchelor, The effect of brownian motion on the bulk stress in a suspension of spherical particles, J. Fluid Mech. **83**, 97 (1977).

[58] A. Einstein, On the theory of the brownian movemoent, Ann. Phys. **324**, 371 (1906).